ACS APPLIED NANO MATERIALS

www.acsanm.org Article

3D Morphology of Bimodal Porous Copper with Nano-Sized and Micron-Sized Pores to Enhance Transport Properties for Functional Applications

Lijie Zou, Mingyuan Ge, Jianming Bai, Chonghang Zhao, Hao Wang, Xianghui Xiao, Hui Zhong, Sanjit Ghose, Wah-Keat Lee, Qiang Shen,* Fei Chen,* and Yu-chen Karen Chen-Wiegart*

Cite This: https://dx.doi.org/10.1021/acsanm.0c01163 Read Online

ABSTRACT: Multiscale porous metals with multiscale porosity from nanometer to micrometer have a high specific surface area and high effective diffusivity for ion transport, thereby enhancing functionalities and extending the applications of porous metals. In this study, the Cu−Fe−Al ternary system was selected as the precursor alloy to construct multiscale, bimodal porous copper by the chemical dealloying method. The effect of the phase composition and initial microstructure of precursor alloys ($Al_xFe_{75-x}Cu_{25}$, x = 10−60) on the three-dimensional (3D) morphology of multiscale porous metals was systematically investigated, with a goal to precisely control the multiscale porous structure. The four crystal structure phases (body-centered cubic (BCC), face-centered cubic (FCC), CsCl type (B2), and monoclinic) in precursor alloys were analyzed by synchrotron X-ray diffraction refinement. The 3D morphology, feature size distribution, and tortuosity of four representative porous Cu after dealloying $Al_xFe_{75-x}Cu_{25}$ (x = 10, 30, 50, and 60) precursor alloys were directly visualized and quantified via advanced synchrotron X-ray nanotomography. The relationship between the phases/crystal structures of precursor alloys and their corresponding porous morphology was established: the micron-sized pores in bimodal porous Cu are formed by dissolving the CuFeAl phase with BCC and monoclinic crystal structures, and the nano-sized pores are formed by dealloying the CuFeAl phase with FCC and B2 crystal structures. The size of the nanoporous structure depends on the ratio between the more noble and more active components in the precursor alloy, while the size of the microporous structure depends on the corresponding phase size in the precursor alloy. The tortuosity results showed that the multiscale porous structure with both nanoporosity and microporosity exhibits lower tortuosity, which will enhance transport properties for functional applications.

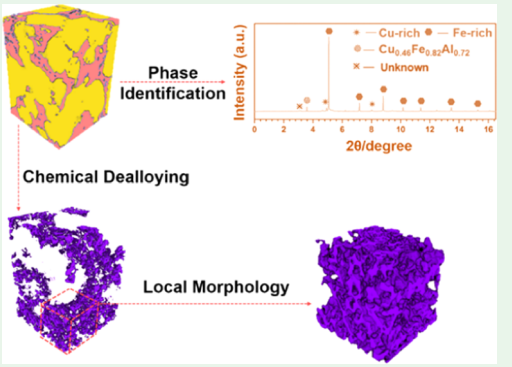

KEYWORDS: *nano-CT, X-ray diffraction, nanoporous, TXM, transmission X-ray microscopy*

1. INTRODUCTION

Multiscale porous metals, with their porous size spanning from nanometers to micrometers, possess unique properties: the high specific surface area enabled by the nanoporous structure provides chemical and physical functionalities;[1−3] simultaneously, the larger microporous structure provides excellent transport properties for long range ion diffusion.[4] Therefore, multiscale porous metals have a wide range of functional applications including electrochemical sensors,[5] heat exchangers,[6] catalysts,[7] and energy storage.[8−10] Multiscale porous metals can be fabricated via sintering, additive manufacturing (AM), templating, and dealloying methods.[11−14] Specifically, dealloying is a versatile method to fabricate multiscale bicontinuous multiscale porous metals.

The dealloying method, involving selective dissolution of more active alloy component(s) and the self-rearrangement of the remaining elements, has attracted great attention and been utilized to fabricate a spongelike, highly interconnected porous structure for functional applications. The dealloying method can be categorized according to different dealloying agents and conditions used to dealloy the precursor alloys: chemical dealloying,[1,15] electrochemical dealloying,[16,17] solid-state interfacial dealloying,[13,18] liquid metal dealloying,[19,20] and vapor phase dealloying;[21,22] each method possesses unique characteristics and applications. In particular, the chemical dealloying method is an effective dealloying method to create multiscale porous metals. Currently, there are three types of chemical dealloying fabrication methods for multiscale porous metals: (1) two-step dealloying method;[23] (2) dealloying of

Received: April 29, 2020
Accepted: July 1, 2020
Published: July 1, 2020

https://dx.doi.org/10.1021/acsanm.0c01163
ACS Appl. Nano Mater. XXXX, XXX, XXX−XXX

intermetallic and metallic elemental phases method,[24] which uses various binary alloy systems as the precursors; and (3) ternary alloy dealloying method,[25] which uses ternary precursor alloys.

Using the two-step dealloying method, Ding et al.[23] fabricated bimodal porous Au by dealloying the Ag−Au alloy. The first dealloying step forms nanoporous Au (NPG) with a pore size of 10−100 nm, which was then electrolessly plated with silver and annealed to simultaneously form the Ag−Au alloy and coarsen the initial NPG; after the second dealloying step, a bimodal porous Au was formed with pore sizes of 1−2 μm and 8 nm. Dealloying of intermetallic and metallic elemental phases method was demonstrated by Song et al.:[24] They fabricated porous Cu containing micron-sized (tens of micrometers) and nano-sized pores (50−200 nm) by dealloying the annealed Cu-75 atom % Al alloy composed of intermetallic $CuAl_2$ and α-Al (Cu) phases. However, dealloying of binary precursor alloys to fabricate multiscale porous metals remains a relatively complicated technique and has limitations in the range of porosity it can produce.

Dealloying of ternary precursor alloys is an effective method to fabricate multiscale porous metals. Zhang et al. fabricated a bimodal nanoporous bimetallic Pt−Au alloy through one-step dealloying of Al−Pt−Au ternary precursor alloys.[26] Subsequently, they fabricated bimodal porous Pd−Au with a finer AuPd nanoporous structure and coarser Pd(Au) nanoporous structure by dealloying the Al−Pd−Au ternary alloy.[27] The multiscale porous Cu−Ti bimetallic electrocatalyst fabricated by Lu et al.[28] shows high hydrogen evolution activity due to the bimodal structure: the micro-scale pores improve the mass transport and the nanopores provide a large surface area for electrocatalytic hydrogen evolution. Qiu et al. designed a bimodal porous Au to enhance the electrocatalytic activity and support the fabrication of an oxidase-based biosensor.[29] Currently, most of the multiscale porous metallic materials prepared by the ternary alloy dealloying method are porous alloys instead of pure porous metals. There are limited studies on pure multiscale porous metals fabricated by dealloying a ternary alloy due to the difficulty in selecting adequate ternary precursor alloy systems and compositions.

Porous Cu has excellent properties: high electrical and thermal conductivities, ductility, nontoxicity, and low cost, which makes porous copper and its derived materials become excellent candidates in a range of applications, such as energy storage and conversion materials, filters, electrochemically or chemically driven actuators, and catalysts.[30] Multiscale porous Cu exhibits high cycling performance as a current collector,[31,32] excellent surface-enhanced Raman scattering (SERS) as a sensor,[33] and high thermal management performance as a heat pipe.[34]

Currently, except the method of dealloying of intermetallic and metallic elemental phases demonstrated by Song et al. mentioned above, other methods have also been used to fabricate multiscale bimodal porous Cu. Shin et al.[35] fabricated a variety of bimodal porous Cu using gas deconvolution in an electrochemical deposition process. $CuSO_4$ and H_2SO_4 are the salts used for porous Cu formation. The bimodal pore size can be adjusted in the ranges of 20−100 μm and 50−300 nm. Some pore size gradient has been observed in this method. Liu et al.[36] fabricated bimodal porous Cu through vacuum dealloying combined with the chemical dealloying method using the $Zn_{70}Cu_{30}$ precursor alloy. The bimodal pore sizes are in the ranges of 0.5−3.5 μm and 200 nm. Luo et al.[31] obtained bimodal porous Cu with irregular microporosity (pore size: 0.5−1 μm) and nanoporosity (pore size: 200−300 nm) by chemical dealloying of the Cu−34Zn−6Al (wt %) ternary precursor alloy. However, the bimodal porous Cu prepared by the latter two methods results in a structure with nano-sized pores distributed on the surface of micron-sized ligaments.

In this study, we investigated bimodal porous Cu with high porosity, nano-sized pores and micron-sized pores fabricated via a simple one-step chemical dealloying method using Cu−Fe−Al ternary alloys as the precursor. The selection of the Cu−Fe−Al ternary alloy system is based on the principle of different mixing enthalpies: when $\Delta H < 0$, the compatibility between elements is good, and when $\Delta H > 0$, the elements are immiscible, which has been discussed in detail in our previous work.[37] To precisely control the structure of the bimodal porous Cu, the effect of the phase composition and microstructure of precursor alloys on the bimodal porous structure was systematically studied. The phase composition was determined via synchrotron X-ray diffraction refinement. Moreover, the three-dimensional (3D) morphology of the precursor Cu−Fe−Al ternary alloy and the corresponding bimodal porous Cu was characterized by advanced synchrotron X-ray nanotomography. The 3D morphological parameters of bimodal porous Cu were quantified to establish the processing-structure correlation for the ternary alloy dealloying method. The specific surface area and transport properties of porous metals are particularly important when they are used as functional materials. Tortuosity (the effective diffusion path length divided by the straight distance) is an important parameter determining the transport properties of porous materials. Therefore, the tortuosity of bimodal porous Cu was quantified in this study. This work provides a guide for porous structure design through controlling phase composition in precursor alloys, so that various multiscale porous structures can be precisely constructed, tailored to specific potential applications.

2. METHODS

2.1. Fabrication of Precursor Alloys and Bimodal Porous Cu and Microstructure Analysis. Metal powders of Cu (99 wt % purity, 1 μm average particle size, Alfa Aesar), Fe (99.5 wt % purity, 8 μm, Alfa Aesar), and Al (99.5 wt % purity, 2 μm, Aladdin Industrial Corporation) with spherical geometry were mixed through two-dimensional low-energy ball milling apparatus (QM-A light ball milling machine, Xianyang, China). The mixed powders were then used to prepare a series of ternary precursor alloys with constant Cu content (25 atom %), adjustable Al content (from 10 to 60 atom %), and Fe content (from 65 to 15 atom %): $Al_xFe_{75}Cu_{25-x}$, x = 10, 20, 30, 40, 50, and 60. Different Cu, Fe, and Al particle sizes were chosen to form homogeneous and dense precursor alloys during the powder metallurgy sintering process. The precursor alloys were sintered at 800 °C for 5 min in vacuum by plasma activated sintering (PAS) facility (ED-PAS 111, Japan) with a sintering pressure of 50 MPa. The precursor alloys (cylindrical shape) with 25 mm diameter and 11 mm thickness after sintering were then machined into cylinders with 5 mm diameter and 10 mm thickness. Subsequently, the chemical dealloying method was applied to fabricate multiscale porous Cu. The Cu−Fe−Al precursor alloys were immersed into the 5 wt % sulfuric acid (H_2SO_4) aqueous solution at 90 °C; when the dealloying completed, no gas bubbles from hydrogen gas evolution emerged in the solution. It takes about 20 h to finish the dealloying process for the alloy (cylindrical shape) with 5 mm diameter and 10 mm thickness. Deionized (DI) water was used to prepare the H_2SO_4 solution. The fully dealloyed samples were immersed in DI water and then ethanol consecutively for about 20 min in each step. The chemistry-

https://dx.doi.org/10.1021/acsanm.0c01163
ACS Appl. Nano Mater. XXXX, XXX, XXX−XXX

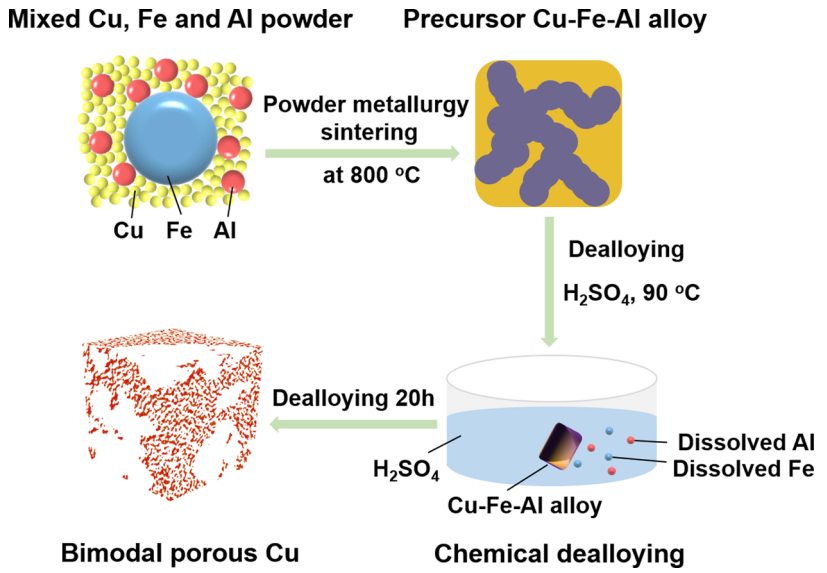

Figure 1. Chemistry-fabrication scheme of a bimodal porous Cu material with nano-sized and micron-sized pores.

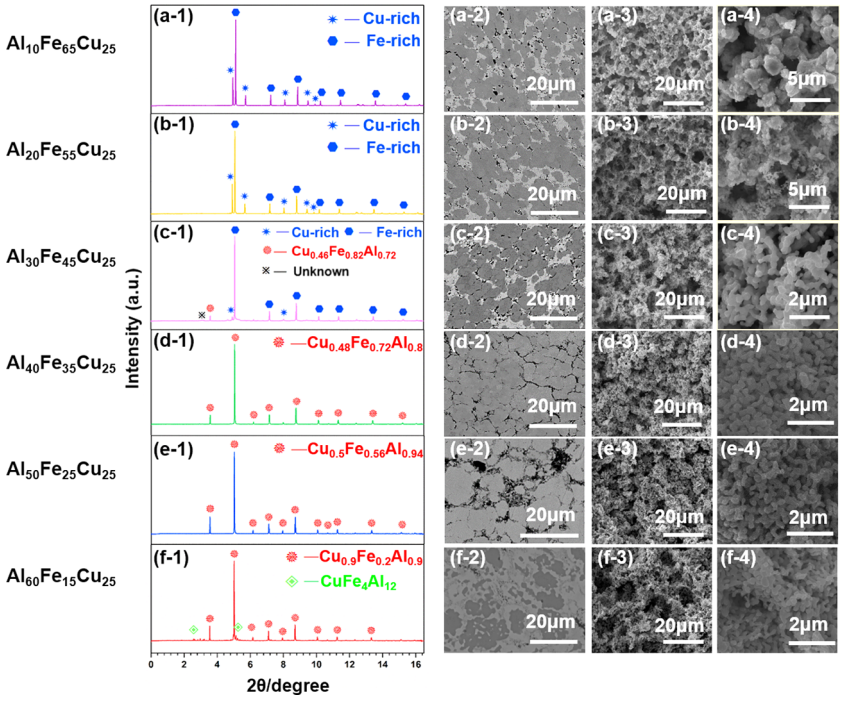

Figure 2. Phase composition and microstructure of precursor alloys and their corresponding porous Cu after dealloying in the 5 wt % H_2SO_4 aqueous solution at 90 °C. The compositions of precursor alloys: (a) $Al_{10}Fe_{65}Cu_{25}$, (b) $Al_{20}Fe_{55}Cu_{25}$, (c) $Al_{30}Fe_{45}Cu_{25}$, (d) $Al_{40}Fe_{35}Cu_{25}$, (e) $Al_{50}Fe_{25}Cu_{25}$, and (f) $Al_{60}Fe_{15}Cu_{25}$. Synchrotron X-ray powder diffraction (XPD) patterns showing phase composition of precursor alloys (a-1–f-1); back-scattering mode of scanning electron microscope (SEM) images showing the microstructure of precursor alloys (a-2–f-2) and corresponding porous Cu (a-3–f-3) and zoom-in view of the porous structure (a-4–f-4).

fabrication scheme of a bimodal porous Cu material with nano-sized and micron-sized pores is shown in Figure 1.

The surface microstructure of Cu–Fe–Al precursor alloys and the cross-sectional microstructure of porous Cu were investigated through scanning electron microscopy (SEM) at the Center for Functional Nanomaterials (CFN) of Brookhaven National Laboratory (BNL).

2.2. Synchrotron X-ray Powder Diffraction (XPD) Characterization. The phase composition of six different Cu–Fe–Al precursor alloys was analyzed at the 28-ID-2 X-ray powder diffraction (XPD) beamline, National Synchrotron Light Source II (NSLS-II), BNL. The detector was a PerkinElmer amorphous silicon flat panel with 2048 (H) × 2048 (V) pixels and 200 μm × 200 μm pixel size. To minimize the effect of the gasket on the diffraction pattern, the beam (52.38 keV) was collimated to about 0.3 mm × 0.2 mm. Pure nickel powder was used as a standard to determine the geometric parameters including the detector-to-sample distance, and the FIT2D program was used for radial integration of the two-dimensional data.[38] Rietveld refinements of the obtained synchrotron diffraction data were performed using the TOPAS V3.0 software.[39]

2.3. Sample Preparation for X-ray Nanotomography Characterization. Based on the phase composition and microstructure analysis results, four representative precursor alloys ($Al_xFe_{75-x}Cu_{25}$, x = 10, 30, 50, 60) and their corresponding porous Cu were selected to conduct X-ray nanotomography characterization.

https://dx.doi.org/10.1021/acsanm.0c01163
ACS Appl. Nano Mater. XXXX, XXX, XXX–XXX

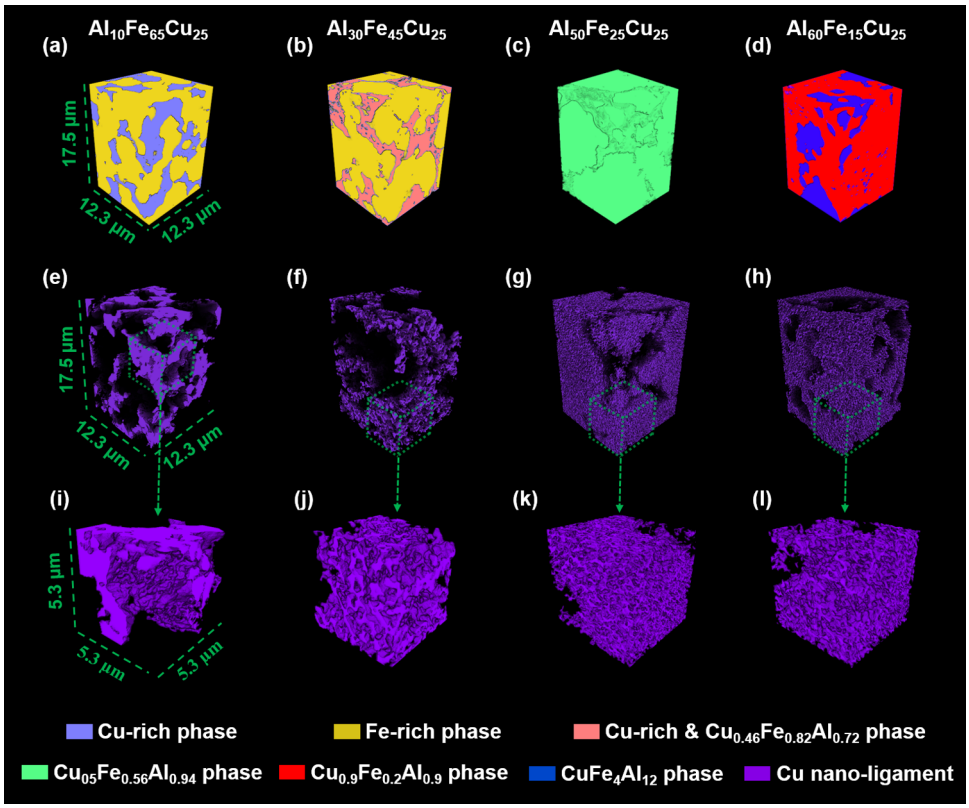

Figure 3. Three-dimensional morphology of Cu−Fe−Al precursor alloys and their corresponding fully dealloyed multiscale porous Cu. X-ray nanotomography reconstruction showing the 3D morphology: (a−d) $Al_{10}Fe_{65}Cu_{25}$, $Al_{30}Fe_{45}Cu_{25}$, $Al_{50}Fe_{25}Cu_{25}$, and $Al_{60}Fe_{15}Cu_{25}$ precursor alloys; (e−h) corresponding multiscale porous Cu with micron- and nano-sized pores; (i)−(l) a "zoom-in" view of the 3D morphology of the nanoporous structure cropped from a volume marked by a green dash rectangle in (e)−(h).

All samples measured in X-ray nanotomography characterization were prepared by focused ion beam (FIB) milling and lifted out at the CFN of BNL. The precursor alloy samples and porous Cu samples were milled into micropillars by 21 nA ion beam current in selected regions, and the surface of the micropillars was cleaned by 2.8 nA ion beam current. Then, the micropillars were cut off by 9.3 nA ion beam, lifted out, and attached to a sharp W pin by Pt deposition following an established procedure published previously.[40] The final cylinders were in the dimensions of 25−30 μm in diameter and ∼50 μm in length.

2.4. Synchrotron Transmission X-ray Microscopy (TXM) Characterization. Synchrotron X-ray nanotomography characterization was conducted at the full-field X-ray imaging (FXI) Beamline 18-ID, NSLS-II, BNL. The FXI beamline has the full-field transmission X-ray microscopy (TXM) at the FXI beamline with the capability to conduct a full 3D nanotomography data set within 1 min of acquisition time.[41] The TXM utilizes a capillary condenser and a 30 nm outermost Fresnel zone plate as an objective lens. The X-ray projection images of the samples were collected on an Andor Neo 5.5 detector with 2560 (H) × 2160 (V) pixels and 6.5 μm × 6.5 μm pixel size. A fly-scan mode was used with a rotation range from 0 to 180°, a rotation speed of 2°/s, and an exposure time of 0.045 s. Finally, 1080 projections images (2 × 2 binned) were recorded with a pixel size of 34 nm. The incident X-ray energy used to conduct this work was at 9.1 keV (above Cu K-edge), 8.95 keV (below Cu K-edge), 7.2 keV (above Fe K-edge), and 7.1 keV (below Fe K-edge).

2.5. Data Processing and Analyzation. The X-ray nanotomography data was reconstructed using the "Gridrec" implementation in Tomopy via a filtered backprojection (FBP) algorithm.[42] The different phases in precursor alloys and pores and ligament in porous Cu in the reconstructed images were segmented using Trainable Weka Segmentation, a machine learning algorithm, in freeware ImageJ.[43,44] A 3D median filter with a kernel size of 2 × 2 × 2 was performed in the segmented images. Commercial software, Avizo (v.9.3 FEI), was used to visualize 3D morphology. A customized Matlab code developed in-house by implementing well-established methods was applied to the segmented 3D images to quantify tortuosity[45] and the size distribution[46] of pores, ligaments, and phases in precursor alloys in three dimensions. The "quasi-Euclidean" voxel neighboring definition algorithm[45] was applied to calculate tortuosity. The volume fraction of pores and ligaments was determined according to voxel counting in the image histogram in freeware ImageJ. Furthermore, mercury porosimetry (AutoPore IV-9500 V1.05) was also used to characterize the pore size distribution of bulk bimodal porous Cu to complement the analysis from X-ray nanotomography, where the sample dimension was limited by the X-ray attenuation and the field of view of the microscope.

3. RESULTS AND DISCUSSION

3.1. Effect of Phase Composition of Precursor Alloys on Morphology of Multiscale Porous Cu. The phase composition and morphology of precursor alloys directly affect the microstructure of corresponding porous metals fabricated by the dealloying method. In this study, Cu, Fe, and Al metal powders with a range of different ratios were used to fabricate precursor Cu−Fe−Al alloys ($Al_xFe_{75-x}Cu_{25}$, x = 10, 20, 30, 40, 50, and 60) with different phase compositions, which creates various porous structures after dealloying. Synchrotron X-ray powder diffraction (XPD) was conducted to identify the phase composition and crystal structure of Cu−Fe−Al precursor alloys via refinement, as shown in Figure 2a-1−f-1. $Fm\bar{3}m$ face-centered cubic (FCC) crystal structure Cu-rich phases and $Im\bar{3}m$ body-centered cubic (BCC) crystal structure Fe-rich phases are observed in both of $Al_{10}Fe_{65}Cu_{25}$ and $Al_{20}Fe_{55}Cu_{25}$ precursor alloys. Therefore, from the backscattering mode of SEM images in Figure 2a-2,b-2, it can be clearly distinguished

https://dx.doi.org/10.1021/acsanm.0c01163
ACS Appl. Nano Mater. XXXX, XXX, XXX−XXX

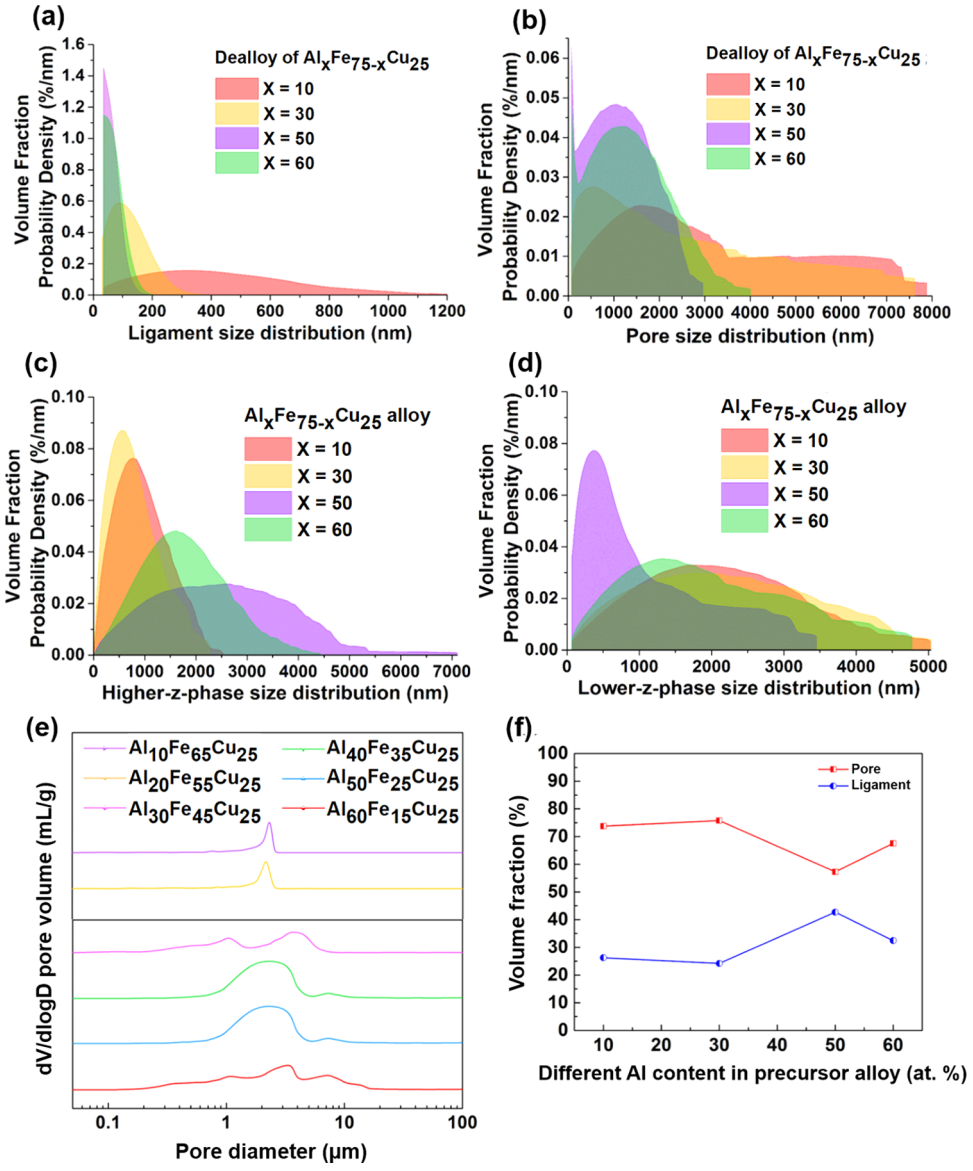

Figure 4. (a) Ligament size distribution and (b) pore size distribution, quantified according to the segmented 3D images of fully dealloyed $Al_xFe_{75-x}Cu_{25}$ (x = 10, 30, 50, and 60) precursor alloys at 90 °C. (c) Higher-Z-phase (which represents the phase with a relatively higher atomic number Z and relatively higher contrast as shown in SEM images in Figure 2) size distribution and (d) lower-Z-phase (which represents the phase with a relatively lower Z and relatively lower contrast as shown in SEM images in Figure 2) size distribution of $Al_{10}Fe_{65}Cu_{25}$, $Al_{30}Fe_{45}Cu_{25}$, $Al_{50}Fe_{25}Cu_{25}$, and $Al_{60}Fe_{15}Cu_{25}$ precursor alloys. (e) Pore size distribution of the bulk sample of fully dealloyed precursor alloys characterized using mercury porosimetry. (f) Volume fraction of 3D morphological parameters: pores and ligaments.

that the bright area is a Cu-rich phase with a relatively higher atomic number (Z), and the dark area is a Fe-rich phase with a relatively lower Z. With the Al content increasing to 30 atom %, the *Pmm* CsCl type (B2) crystal structure $Cu_{0.45}Fe_{0.7}Al_{0.85}$ phase appears, and there is also a very small amount of unknown phase that cannot be identified because of the low intensity in its X-ray signal, so that there are four phases in the $Al_{30}Fe_{45}Cu_{25}$ precursor alloy, as shown in Figure 2c-1; note that here the intensity of the Cu-rich phase becomes quite low. With the continuing increase of the Al content to 40−50 atom %, there is only a B2 crystal structure $Cu_{0.48}Fe_{0.72}Al_{0.8}$ phase in the $Al_{40}Fe_{35}Cu_{25}$ alloy and a B2 crystal structure $Cu_{0.50}Fe_{0.56}Al_{0.94}$ phase in the $Al_{50}Fe_{25}Cu_{25}$ precursor alloy. Because of the less amount of densification of $Cu_{0.48}Fe_{0.72}Al_{0.8}$ and $Cu_{0.5}Fe_{0.56}Al_{0.94}$ phases, some continuous cracks and voids can be observed in $Al_{40}Fe_{35}Cu_{25}$ and $Al_{50}Fe_{25}Cu_{25}$ precursor alloys, seen as the dark area in Figure 2d-2,e-2. In the precursor with 60 atom % of Al, the B2 crystal structure $Cu_{0.9}Fe_{0.2}Al_{0.9}$ phase (the phase with a relatively higher Z) and the $C/2m$ monoclinic crystal structure $CuFe_4Al_{12}$ intermetallic phase (the phase with a relatively lower Z) are formed in the $Al_{60}Fe_{15}Cu_{25}$ precursor alloy. The synchrotron X-ray powder diffraction (XPD) refinement results of six different precursor alloys are shown in Supporting Information Figure S1 and Table S1.

After chemical dealloying using the 5 wt % sulfuric acid (H_2SO_4) aqueous solution at 90 °C, all of the six precursor alloys are fully dealloyed (as shown in Figure S2) and form a multiscale porous structure, regardless of the composition and number of phases contained in the precursor alloy. However, the pore size of the microporous structure formed by dealloying of $Al_{40}Fe_{35}Cu_{25}$ and $Al_{50}Fe_{25}Cu_{25}$ precursor alloys is smaller than the other compositions, as shown in Figure 2a-

https://dx.doi.org/10.1021/acsanm.0c01163
ACS Appl. Nano Mater. XXXX, XXX, XXX−XXX

3−f-3. For the precursor alloy with low content of Al, only little amount of nanoporous structure formed on the surface of the micron-sized pore's ligaments. When the Al content increases to 30 % or even higher than 30 atom %, the whole ligaments of micron-sized pores become a nanoporous structure.

Synchrotron X-ray nanotomography characterizes the 3D morphology of four representative Cu−Fe−Al precursor alloys ($Al_xFe_{75-x}Cu_{25}$, x = 10, 30, 50, 60) and their corresponding fully dealloyed multiscale porous Cu, as shown in Figure 3. In Figure 3a, the Cu-rich phase (light blue color) formed in the $Al_{10}Fe_{65}Cu_{25}$ alloy exhibits a 3D continuous structure. The volume of the Fe-rich phase (yellow color) in this alloy is larger than that of the Cu-rich phase. For the $Al_{30}Fe_{45}Cu_{25}$ alloy, the unknown phase will not be considered in the following discussion due to the low content. Because the volume percent of the Cu-rich phase in the $Al_{30}Fe_{45}Cu_{25}$ alloy is quite low (as shown in Table S1) and beyond the limits of accurate segmentation, we labeled the Cu-rich and $Cu_{0.45}Fe_{0.7}Al_{0.85}$ phases as a mixed phase, marked with pink color (Figure 3b). When the Al content increases to 50 atom %, only the $Cu_{0.5}Fe_{0.56}Al_{0.94}$ phase (light green color) and cracks and voids (black color) can be observed in the precursor alloy. Moreover, we can observe cracks and voids in the structure likely caused by incomplete densification during the sintering process. In the $Al_{60}Fe_{15}Cu_{25}$ alloy, in addition to the $Cu_{0.9}Fe_{0.2}Al_{0.9}$ phase (red color), there is also the $CuFe_4Al_{12}$ phase (dark blue color), whose shape and size are not homogeneous.

The difference of 3D morphology between Cu−Fe−Al precursor alloys leads to a variety of multiscale porous structures after dealloying. Through comparing the chemical activity and 3D morphology of different phases in precursor alloys and the 3D morphology of the porous structure, it can be identified that the micron-sized pores in multiscale porous Cu are formed due to the dissolution of the Fe-rich phase in both $Al_{10}Fe_{65}Cu_{25}$ alloy and $Al_{30}Fe_{45}Cu_{25}$ alloy, and the $CuFe_4Al_{12}$ phase in the $Al_{60}Fe_{15}Cu_{25}$ alloy. With the dissolution of the Al and Fe active components, the active (less noble) components (Fe and Al)-rich phase forms a nanoporous structure first; then, the undissolved Fe and Al components in the nano-ligaments are gradually dissolved until the dissolution is complete. Because these active component-rich phases contain no or little amount of Cu, the Cu content is not sufficient to form a continuous network structure after the dissolution of Fe and Al, and thus a microporous structure forms. The specific formation mechanism of micron-sized pores has been discussed in our previous work.[37] The nanoporous structure was formed by dealloying of other phases in the four representative precursor alloys: Cu-rich, $Cu_{0.45}Fe_{0.7}Al_{0.85}$, $Cu_{0.5}Fe_{0.56}Al_{0.94}$, and $Cu_{0.9}Fe_{0.2}Al_{0.9}$ phases. Note that while micron-sized pores can also be observed in porous Cu after dealloying of the $Al_{50}Fe_{25}Cu_{25}$ alloy, which has just one phase, due to the contribution of the initial voids in the precursor alloy, the morphology of the microporous structure in Figure 3g is similar to the voids in Figure 3c. The porous Cu fabricated by dealloying of the $Al_{10}Fe_{65}Cu_{25}$ alloy exhibits the most homogeneous microporous structure, but there is only little amount of nanoporous structure formed due to the low content of Al. With the Al content increasing to 30 atom % or higher in precursor alloys, all of the micron-sized ligaments in their corresponding porous Cu are composed of a nanoporous structure, which can be seen in Figure 3f−h, with the zoom-in view in Figure 3j−l. The multiscale porous Cu formed by dealloying the $Al_{50}Fe_{25}Cu_{25}$ alloy possesses the largest volume of the nanoporous structure; this is because only the $Cu_{0.5}Fe_{0.56}Al_{0.94}$ phase forms nanopores in the $Al_{50}Fe_{25}Cu_{25}$ alloy, and the volume of initial cracks and voids caused by incomplete sintering densification is relatively low. Moreover, comparing Figure 3k,l with Figure 3j from tomography analysis, the nano-ligament size of porous Cu dealloyed from the $Al_{50}Fe_{25}Cu_{25}$ and $Al_{60}Fe_{15}Cu_{25}$ alloys is found to be smaller than that dealloyed from the $Al_{30}Fe_{45}Cu_{25}$ alloy.

3.2. Quantification of Morphological Parameters of Multiscale Porous Structure. To further explore the relationship between precursor alloys and the multiscale porous structure, the 3D morphology of the four representative precursor alloys $Al_{10}Fe_{65}Cu_{25}$, $Al_{30}Fe_{45}Cu_{25}$, $Al_{50}Fe_{25}Cu_{25}$, and $Al_{60}Fe_{15}Cu_{25}$ and their corresponding multiscale porous Cu are compared here through quantitative calculation of different morphological parameters, as shown in Figure 4. From Figure 4a, it can be found that with the increase of the Al content in precursor alloys, the ligament size of their corresponding porous Cu decreases gradually. The ligament size of porous Cu after dealloying of the $Al_{60}Fe_{15}Cu_{25}$ alloy is just ∼100 nm. In contrast, the ligament size of porous Cu after dealloying of the $Al_{10}Fe_{65}Cu_{25}$ alloy shows a wider distribution: from nanometer to micrometer. The pore size distribution of porous Cu in Figure 4b shows that the pore size of dealloyed $Al_{10}Fe_{65}Cu_{25}$ is primarily in the micrometer size range, with only little amount of nano-sized pores. The other three types of porous Cu show a distinct multiscale bimodal porous structure. The nano-sized pores of the multiscale porous Cu after dealloying of $Al_{50}Fe_{25}Cu_{25}$ and $Al_{60}Fe_{15}Cu_{25}$ alloys are quite similar and smallest. With the Al content of the precursor alloy decreasing to 30 atom %, nano-sized pores become larger. According to the prior discussions, we know that the nanoporous structure from dealloying of $Al_{50}Fe_{25}Cu_{25}$ and $Al_{60}Fe_{15}Cu_{25}$ alloys is formed by dealloying the B2 crystal structure phase, and that the nanoporous structure from dealloying of $Al_{10}Fe_{65}Cu_{25}$ and $Al_{30}Fe_{45}Cu_{25}$ alloys is formed by dealloying the FCC crystal structure phase. Therefore, it indicates that the pore size through the dealloying B2 crystal structure phase is smaller than the dealloying fcc crystal structure phase. Meanwhile, the size distribution of micron-sized pores in different porous Cu does not follow a specific trend, and it mainly depends on the size of the corresponding dissolving phases in precursor alloys because they have the same size distribution trend. This can be further understood through results in Figure 4c,d.

Figure 4c shows the size distribution of the phases in precursor alloys that form a nanoporous structure after dealloying: the Cu-rich phase (light blue color in Figure 3a) in the $Al_{10}Fe_{65}Cu_{25}$ alloy, the Cu-rich and $Cu_{0.46}Fe_{0.82}Al_{0.72}$ mixed phase (pink color in Figure 3b) in the $Al_{30}Fe_{45}Cu_{25}$ alloy, the $Cu_{0.5}Fe_{0.56}Al_{0.94}$ phase (light green color in Figure 3c) in the $Al_{50}Fe_{25}Cu_{25}$ alloy, and the $Cu_{0.9}Fe_{0.2}Al_{0.9}$ (red color in Figure 3d) phase in the $Al_{60}Fe_{15}Cu_{25}$ alloy, which is denoted as the higher-Z phase (it is named on the basis of the relative atomic number Z and contrast in SEM images in Figure 2). The size distribution of the phases that form a microporous structure is shown in Figure 4d: Fe-rich phase (yellow color in Figure 3a,b) in $Al_{10}Fe_{65}Cu_{25}$ and $Al_{30}Fe_{45}Cu_{25}$ alloys, the cracks and voids (black uneven area in Figure 3c) in the $Al_{50}Fe_{25}Cu_{25}$ alloy, and the $CuFe_4Al_{12}$ phase (dark blue color in Figure 3d) in the $Al_{60}Fe_{15}Cu_{25}$ alloy, which is denoted as

https://dx.doi.org/10.1021/acsanm.0c01163
ACS Appl. Nano Mater. XXXX, XXX, XXX−XXX

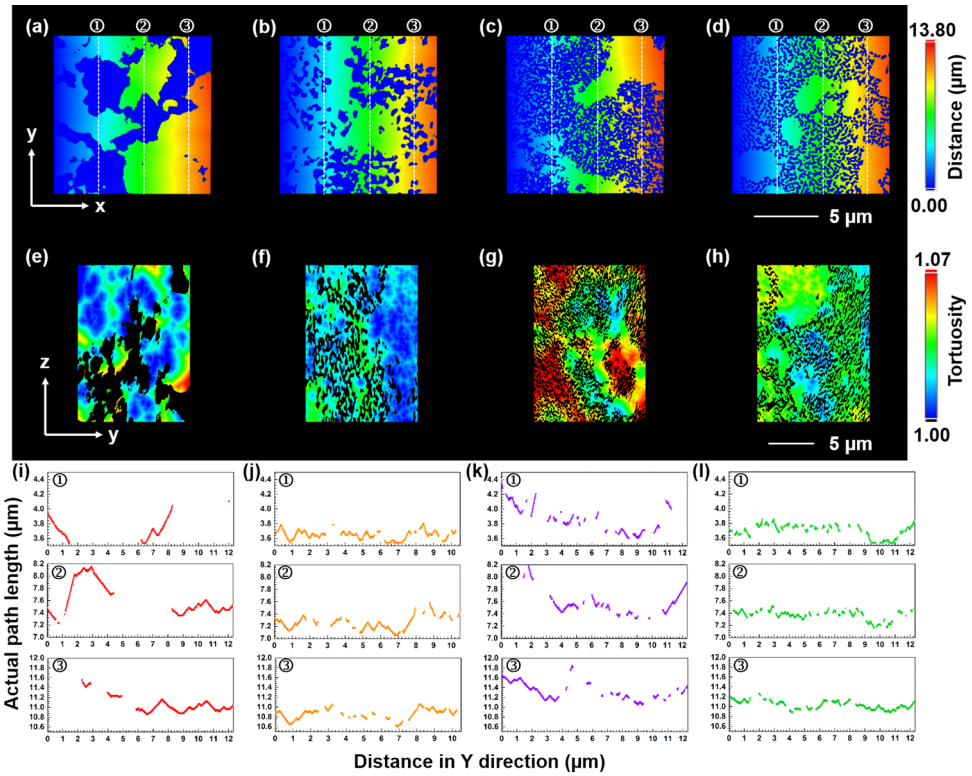

Figure 5. Tortuosity, 3D distance map, and distance profiles at three specific positions based on geometric propagation within the pore phase of multiscale porous Cu after dealloying of $Al_xFe_{75-x}Cu_{25}$ (x = 10, 30, 50, and 60) precursor alloys. (a–d) Three-dimensional distance map propagating along the positive x-direction, (e–h) spatial distribution maps of tortuosity in the x-direction, and (i–l) distance profiles showing the actual diffusion path length of multiscale porous Cu at three different x locations as indicated in (a)–(d).

lower-Z phase. The average size of the higher-Z phase in $Al_{10}Fe_{65}Cu_{25}$ and $Al_{30}Fe_{45}Cu_{25}$ alloys is about 1 μm and smaller than the other two precursor alloys. The higher-Z phase in the $Al_{50}Fe_{25}Cu_{25}$ alloy is the largest, which is consistent with the morphology in Figure 3. In contrast, the lower-Z phase in the $Al_{50}Fe_{25}Cu_{25}$ alloy shows the smallest size, including voids from nanometer to micrometer because it is formed from incomplete sintering densification. The size of the lower-Z phase that forms micron-sized pores after dealloying of $Al_{50}Fe_{25}Cu_{25}$, $Al_{60}Fe_{15}Cu_{25}$, $Al_{30}Fe_{45}Cu_{25}$, and $Al_{10}Fe_{65}Cu_{25}$ alloys increases gradually, which has the same trend as the micron-sized pore shown in Figure 4b. Because of the sample volume size limitation here in X-ray nanotomography, it cannot evaluate the distribution of micron-sized pores accurately. Therefore, the pore size distribution of bulk porous Cu was characterized using mercury porosimetry, as shown in Figure 4e. The volume fraction of pores should be similar in this series of Cu–Fe–Al precursor alloys due to the same content of Cu. However, in Figure 4f, the volume fraction of pores after dealloying of the $Al_{50}Fe_{25}Cu_{25}$ alloy is lower than the other samples. This may be due to the region-to-region variation when selecting the sample volume for quantitative calculation because the size of initial cracks and voids in the $Al_{50}Fe_{25}Cu_{25}$ alloy is quite inhomogeneous, as shown in Figure 4d.

The effective diffusivity and conductivity for porous media can be quantitatively reflected through an important geometric parameter—tortuosity, which is the ratio between a tortuous path distance and a straight distance.[45,47] Three-dimensional distance maps are shown in Figure 5 to directly quantify and visualize the tortuosity based on geometric propagation. Although all three orthogonal directions, each with both positive and negative propagating directions, were calculated, only the 3D path distance maps along the positive direction of the x-axis are displayed here as a representation because the multiscale porous Cu is a three-dimensional homogeneous structure.[48] In Figure 5a–d, the color bar shows the actual propagating path distance. The white lines marked in the 3D path distance maps are three different x locations along the y-direction, which represents the straight distance of 3.52, 7.04, and 10.56 μm, respectively.

Combining 3D path distance maps in Figure 5a–d and distance profiles in Figure 5i–l, it can be found that the more homogeneous of the ligament size distribution, the more homogeneous of the actual path distance along the y-direction in the three selected specific x locations in porous Cu. Therefore, the porous Cu from dealloying the $Al_{10}Fe_{65}Cu_{25}$ alloy shows the most inhomogeneous propagation front, which is due to the existence of a small amount of nanoporous structure on the surface of some micro-ligaments. However, the ligaments of the Cu porous structure from dealloying $Al_{30}Fe_{45}Cu_{25}$ and $Al_{60}Fe_{15}Cu_{25}$ precursor alloys are quite homogeneous and all in nano size, so that the actual propagation front in these alloys is more uniform, compared with the microporous structure from dealloying the $Al_{10}Fe_{65}Cu_{25}$ alloy. From the spatial distribution maps of tortuosity in the x-direction in Figure 5e–h, the tortuosity of all of these four porous Cu is relatively low, with the highest tortuosity ~1.07, which is beneficial for ionic transport through the porous structure. Bae et al. have demonstrated this via artificially engineered battery electrodes.[47] The porous Cu after dealloying of the $Al_{50}Fe_{25}Cu_{25}$ alloy exhibits the highest

https://dx.doi.org/10.1021/acsanm.0c01163
ACS Appl. Nano Mater. XXXX, XXX, XXX–XXX

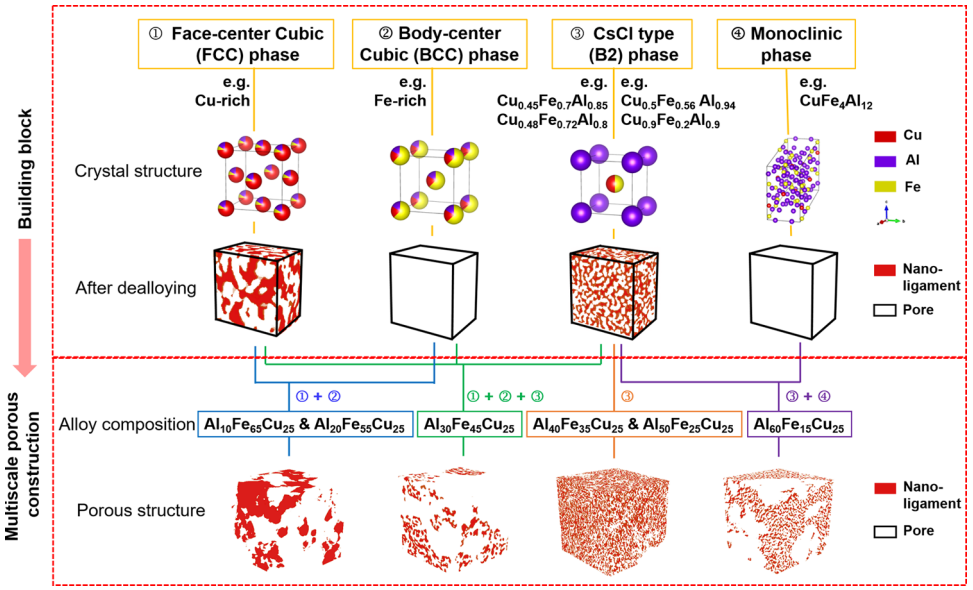

Figure 6. Design concept of various multiscale porous Cu constructions with specific morphology through selecting different building blocks. The $Fm\bar{3}m$, $Im\bar{3}m$, $Pm\bar{3}m$, and $C2/m$ crystal structure phases and their corresponding morphology after dealloying are considered as the building blocks.

tortuosity because it owns the lowest volume fraction of the micron-sized pore; the tortuosity of the other three porous structures is lower, which shows that the micron-sized pores can compensate the increase of the diffusion path length due to nanoporosity, facilitating diffusion within a porous structure.

Finally, the relationship between individual typical phases and their corresponding porous morphology after dealloying is summarized in Figure 6. The FCC and B2 structure phases with higher noble metallic atom content (Cu in this study) will form a nanoporous structure after dealloying; among them, the B2 structure phase has relatively lower noble atom content, so that the nanopores and nano-ligaments size will be smaller. However, when the content of the noble metallic atom in a precursor phase is too low to form a continuous network structure after dealloying, the whole phase will be fully dissolved and form a porous structure with the same size as the corresponding precursor phase, for example, BCC and monoclinic structure phase. Therefore, if the FCC, BCC, B2, and monoclinic crystal structure phases and their corresponding morphology after dealloying are considered as the "building blocks", various multiscale porous Cu with specific morphology can be designed through mixing different individual "building" blocks. Therefore, $Al_{10}Fe_{65}Cu_{25}$, $Al_{20}Fe_{55}Cu_{25}$, $Al_{30}Fe_{45}Cu_{25}$, and $Al_{60}Fe_{15}Cu_{25}$ alloys will form a bimodal porous structure after dealloying, and their pore size and ligament size will decrease gradually. Because $Al_{40}Fe_{35}Cu_{25}$ and $Al_{50}Fe_{25}Cu_{25}$ alloys only have one $Cu_4Fe_6Al_{12}$ phase, they will theoretically form a single-modal nanoporous structure. However, by introducing voids from incomplete densification during sintering, $Al_{40}Fe_{35}Cu_{25}$ and $Al_{50}Fe_{25}Cu_{25}$ alloys can also formed a bimodal porous structure after dealloying.

4. CONCLUSIONS

In this study, different types of multiscale porous Cu with both micron-sized pores and nano-sized pores were successfully fabricated through chemical dealloying of a series of Cu−Fe−Al precursor alloys: $Al_xFe_{75-x}Cu_{25}$, x = 10, 20, 30, 40, 50, and 60. According to the phase composition and 3D morphology of four representative precursor alloys and corresponding porous Cu, it can be identified that FCC and B2 crystal structure phases will form a nanoporous structure after dealloying; meanwhile, BCC and monoclinic crystal structure phases will be dissolved to form microporosity. By combining the analysis of 3D morphology and quantifying 3D morphological parameters, we showed that the size of the nano-sized pore is determined by the component of phase in precursor alloys: the pore size formed by dealloying of the B2 crystal structure phase is smaller than that formed by dealloying of the FCC crystal structure phase, while the size of the micron-sized pore only depends on the initial size of BCC and monoclinic crystal structure phases in precursor alloys. In the case of incomplete sintering, the initial cracks and voids in precursor alloys will also have an impact on the size of microporosity. The multiscale porous Cu exhibits a uniform diffusion propagation front, with a relatively low tortuosity of up to ~1.07. The low tortuosity of bimodal porous Cu is beneficial to enhance the transport properties for functional applications. This work provides a guideline to precisely control the multiscale Cu porous structure formed by dealloying of multiphase ternary Cu−Fe−Al alloys via adjusting the phase compositions. Various porous structures can be designed according to specific applications for optimal performance. Exploring and further testing the design principle to other ternary alloy systems including Cu ternary alloys in the future would be beneficial.

■ ASSOCIATED CONTENT

Supporting Information

The Supporting Information is available free of charge at https://pubs.acs.org/doi/10.1021/acsanm.0c01163.

Further information on experimental methods; further information on refinement analysis results; composition of bimodal porous Cu after dealloying of Cu−Fe−Al alloys; average size from the pore size distribution by Gaussian fitting (PDF)

https://dx.doi.org/10.1021/acsanm.0c01163
ACS Appl. Nano Mater. XXXX, XXX, XXX−XXX

AUTHOR INFORMATION

Corresponding Authors

Qiang Shen − *State Key Laboratory of Advanced Technology for Materials Synthesis and Processing, Wuhan University of Technology, Wuhan 430070, China*; Email: sqqf@whut.edu.cn

Fei Chen − *State Key Laboratory of Advanced Technology for Materials Synthesis and Processing, Wuhan University of Technology, Wuhan 430070, China*; orcid.org/0000-0001-9643-7191; Email: chenfei027@whut.edu.cn

Yu-chen Karen Chen-Wiegart − *Department of Materials Science and Chemical Engineering, Stony Brook University, Stony Brook, New York 11794, United States; National Synchrotron Light Source II, Brookhaven National Laboratory, Upton, New York 11973, United States*; orcid.org/0000-0003-4445-2159; Email: Karen.Chen-Wiegart@stonybrook.edu

Authors

Lijie Zou − *State Key Laboratory of Advanced Technology for Materials Synthesis and Processing, Wuhan University of Technology, Wuhan 430070, China; Department of Materials Science and Chemical Engineering, Stony Brook University, Stony Brook, New York 11794, United States*; orcid.org/0000-0001-9946-6537

Mingyuan Ge − *National Synchrotron Light Source II, Brookhaven National Laboratory, Upton, New York 11973, United States*

Jianming Bai − *National Synchrotron Light Source II, Brookhaven National Laboratory, Upton, New York 11973, United States*; orcid.org/0000-0002-0575-2987

Chonghang Zhao − *Department of Materials Science and Chemical Engineering, Stony Brook University, Stony Brook, New York 11794, United States*; orcid.org/0000-0002-3538-6199

Hao Wang − *State Key Laboratory of Advanced Technology for Materials Synthesis and Processing, Wuhan University of Technology, Wuhan 430070, China*

Xianghui Xiao − *National Synchrotron Light Source II, Brookhaven National Laboratory, Upton, New York 11973, United States*

Hui Zhong − *Department of Joint Photon Science Institute, Stony Brook University, Stony Brook, New York 11794, United States*

Sanjit Ghose − *National Synchrotron Light Source II, Brookhaven National Laboratory, Upton, New York 11973, United States*

Wah-Keat Lee − *National Synchrotron Light Source II, Brookhaven National Laboratory, Upton, New York 11973, United States*

Complete contact information is available at: https://pubs.acs.org/10.1021/acsanm.0c01163

Author Contributions

L.Z., Y.-c.K.C.-W, F.C., and Q.S. developed the research idea. L.Z. and Y.-c.K.C.-W. wrote user proposals for the use of FXI and XPD beamlines at NSLS-II and equipment at CFN; H.W. prepared a precursor alloy under the supervision of F.C.; L.Z. conducted dealloying and SEM analysis; L.Z. and C.Z. prepared samples for FXI beamtime. M.G., X.X., and W.-K.L. commissioned and set up the FXI beamline. L.Z., C.Z., M.G., X.X., W.-K.L., and Y.-c.K.C.-W conducted the FXI experiment and preliminary data analysis during the experiment together. J.B., H.Z., and S.G. set up the XPD beamline and assisted with data collection. L.Z. conducted FXI data analysis with inputs and guidance from M.G., C.Z., and Y.-c.K.C.-W. and XPD data analysis with guidance from J.B.; F.C. and Y.-c.K.C.-W. provided scientific insights on data interpretation and mechanistic understanding. L.Z. and Y.-c.K.C.-W. prepared the manuscript, with inputs from other co-authors.

Notes

The authors declare no competing financial interest.

ACKNOWLEDGMENTS

The authors thank Gwen Wright (Center for Functional Nanomaterials, CFN) for assisting SEM, Fernando Camino (CFN) for EDS support and sample preparation with a FIB−SEM, and Kim Kisslinger for assisting characterization and sample preparation at CFN. The authors also thank Michale Maklary (NSLS-II) for sample machining. This research used resources, full-field X-ray imaging beamline (FXI, 18-ID) and the powder diffraction beamline (XPD, 28-ID-2) of the National Synchrotron Light Source II, a U.S. Department of Energy (DOE) Office of Science User Facility operated for the DOE Office of Science by Brookhaven National Laboratory under Contract No. DE-SC0012704. This research used resources of the Center for Functional Nanomaterials, which is a U.S. DOE Office of Science Facility, at Brookhaven National Laboratory under Contract No. DE-SC0012704. This work is also financially supported by the National Key Research and Development Program of China (Nos. 2018YFB0905600 and 2017YFB0310400), the National Natural Science Foundation of China (Nos. 51472188 and 51521001), Fundamental Research Funds for the Central Universities in China, State Key Laboratory of Advanced Electromagnetic Engineering and Technology (Huazhong University of Science and Technology), and the "111" project (No. B13035). This material is based upon the work supported by the National Science Foundation under Grant no. DMR-1752839. Y.-c.K.C.-W. acknowledges the support provided via the Faculty Early Career Development Program (CAREER) program and Metals and Metallic Nanostructures program of National Science Foundation. C.Z. and Y.-c.K.C.-W. are grateful for the support of a student fellowship by the Joint Photon Science Institute at Stony Brook University, jointly proposed by Y.-c.K.C.-W. as PI and Yong Chu as co-PI and Juergen Thieme and W.-K.L. as collaborators. Y.-c.K.C.-W. group members are acknowledged for conducting the FXI and XPD beamtime experiment together and assisting with preliminary analysis: Xiaoyang Liu, Cheng-Hung Lin, and Qingkun Meng. L.Z. is grateful for the support of the State Scholarship Fund by the China Scholarship Council (CSC).

REFERENCES

(1) Yun, Q.; He, Y. B.; Lv, W.; Zhao, Y.; Li, B.; Kang, F.; Yang, Q. H. Chemical Dealloying Derived 3D Porous Current Collector for Li Metal Anodes. *Adv. Mater.* **2016**, *28*, 6932−6939.

(2) Zhao, H.; Lei, D.; He, Y.-B.; Yuan, Y.; Yun, Q.; Ni, B.; Lv, W.; Li, B.; Yang, Q.-H.; Kang, F.; Lu, J. Compact 3D Copper with Uniform Porous Structure Derived by Electrochemical Dealloying as Dendrite-Free Lithium Metal Anode Current Collector. *Adv. Energy Mater.* **2018**, *8*, No. 1800266.

(3) Ding, Y.; Chen, M. Nanoporous Metals for Catalytic and Optical Applications. *MRS Bull.* **2009**, *34*, 569−576.

https://dx.doi.org/10.1021/acsanm.0c01163
ACS Appl. Nano Mater. XXXX, XXX, XXX−XXX

(4) Wada, T.; Geslin, P.-A.; Kato, H. Preparation of hierarchical porous metals by two-step liquid metal dealloying. *Scr. Mater.* **2018**, *142*, 101−105.
(5) Liu, Z.; Du, J.; Qiu, C.; Huang, L.; Ma, H.; Shen, D.; Ding, Y. Electrochemical sensor for detection of p-nitrophenol based on nanoporous gold. *Electrochem. Commun.* **2009**, *11*, 1365−1368.
(6) Tuchinskiy, L. Novel Manufacturing Process for Metal and Ceramic Microhoneycombs. *Adv. Eng. Mater.* **2008**, *10*, 219−222.
(7) Zhang, J.; Li, C. M. Nanoporous metals: fabrication strategies and advanced electrochemical applications in catalysis, sensing and energy systems. *Chem. Soc. Rev.* **2012**, *41*, 7016−7031.
(8) Joo, S. H.; Choi, S. J.; Oh, I.; Kwak, J.; Liu, Z.; Terasaki, O.; Ryoo, R. Ordered nanoporous arrays of carbon supporting high dispersions of platinum nanoparticles. *Nature* **2001**, *412*, 169−172.
(9) An, Y.; Fei, H.; Zeng, G.; Xu, X.; Ci, L.; Xi, B.; Xiong, S.; Feng, J.; Qian, Y. Vacuum distillation derived 3D porous current collector for stable lithium−metal batteries. *Nano Energy* **2018**, *47*, 503−511.
(10) Shin, H. C.; Liu, M. Three-Dimensional Porous Copper-Tin Alloy Electrodes for Rechargeable Lithium Batteries. *Adv. Funct. Mater.* **2005**, *15*, 582−586.
(11) Banhart, J. Light-Metal Foams-History of Innovation and Technological Challenges. *Adv. Eng. Mater.* **2013**, *15*, 82−111.
(12) Song, T.; Yan, M.; Qian, M. The enabling role of dealloying in the creation of specific hierarchical porous metal structures—A review. *Corros. Sci.* **2018**, *134*, 78−98.
(13) Atwater, M. A.; Guevara, L. N.; Darling, K. A.; Tschopp, M. A. Solid State Porous Metal Production: A Review of the Capabilities, Characteristics, and Challenges. *Adv. Eng. Mater.* **2018**, *20*, No. 1700766.
(14) Juarez, T.; Biener, J.; Weissmüller, J.; Hodge, A. M. Nanoporous Metals with Structural Hierarchy: A Review. *Adv. Eng. Mater.* **2017**, *19*, No. 1700389.
(15) Liu, W. B.; Zhang, S. C.; Li, N.; Zheng, J. W.; Xing, Y. L. A facile one-pot route to fabricate nanoporous copper with controlled hierarchical pore size distributions through chemical dealloying of Al−Cu alloy in an alkaline solution. *Microporous Mesoporous Mater.* **2011**, *138*, 1−7.
(16) Zhang, Q.; Wang, X.; Qi, Z.; Wang, Y.; Zhang, Z. A benign route to fabricate nanoporous gold through electrochemical dealloying of Al−Au alloys in a neutral solution. *Electrochim. Acta* **2009**, *54*, 6190−6198.
(17) Huang, J. F.; Sun, I. W. Fabrication and Surface Functionalization of Nanoporous Gold by Electrochemical Alloying/Dealloying of Au-Zn in an Ionic Liquid, and the Self-Assembly ofL-Cysteine Monolayers. *Adv. Funct. Mater.* **2005**, *15*, 989−994.
(18) Zhao, C.; Kisslinger, K.; Huang, X.; Lu, M.; Camino, F.; Lin, C.-H.; Yan, H.; Nazaretski, E.; Chu, Y.; Ravel, B.; Liu, M.; Chen-Wiegart, Y.-C. K. Bi-continuous pattern formation in thin films via solid-state interfacial dealloying studied by multimodal characterization. *Mater. Horiz.* **2019**, *6*, 1991−2002.
(19) Wada, T.; Kato, H. Three-dimensional open-cell macroporous iron, chromium and ferritic stainless steel. *Scr. Mater.* **2013**, *68*, 723−726.
(20) Mokhtari, M.; Le Bourlot, C.; Adrien, J.; Bonnin, A.; Wada, T.; Duchet-Rumeau, J.; Kato, H.; Maire, E. Microstructure characterization by X-ray tomography and EBSD of porous FeCr produced by liquid metal dealloying. *Mater. Charact.* **2018**, *144*, 166−172.
(21) Lu, Z.; Li, C.; Han, J.; Zhang, F.; Liu, P.; Wang, H.; Wang, Z.; Cheng, C.; Chen, L.; Hirata, A.; Fujita, T.; Erlebacher, J.; Chen, M. Three-dimensional bicontinuous nanoporous materials by vapor phase dealloying. *Nat. Commun.* **2018**, *9*, No. 276.
(22) Han, J.; Li, C.; Lu, Z.; Wang, H.; Wang, Z.; Watanabe, K.; Chen, M. Vapor phase dealloying: A versatile approach for fabricating 3D porous materials. *Acta Mater.* **2019**, *163*, 161−172.
(23) Ding, Y.; Erlebacher, J. Nanoporous Metals with Controlled Multimodal Pore Size Distribution. *J. Am. Chem. Soc.* **2003**, *125*, 7772−7773.
(24) Song, T.; Yan, M.; Shi, Z.; Atrens, A.; Qian, M. Creation of bimodal porous copper materials by an annealing-electrochemical dealloying approach. *Electrochim. Acta* **2015**, *164*, 288−296.
(25) Snyder, J.; Asanithi, P.; Dalton, A. B.; Erlebacher, J. Stabilized Nanoporous Metals by Dealloying Ternary Alloy Precursors. *Adv. Mater.* **2008**, *20*, 4883−4886.
(26) Xu, J.; Zhang, C.; Wang, X.; Ji, H.; Zhao, C.; Wang, Y.; Zhang, Z. Fabrication of bi-modal nanoporous bimetallic Pt−Au alloy with excellent electrocatalytic performance towards formic acid oxidation. *Green Chem.* **2011**, *13*, 1914−1922.
(27) Wang, X.; Sun, J.; Zhang, C.; Kou, T.; Zhang, Z. On the Microstructure, Chemical Composition, and Porosity Evolution of Nanoporous Alloy through Successive Dealloying of Ternary Al−Pd−Au Precursor. *J. Phys. Chem. C* **2012**, *116*, 13271−13280.
(28) Lu, Q.; Hutchings, G. S.; Yu, W.; Zhou, Y.; Forest, R. V.; Tao, R.; Rosen, J.; Yonemoto, B. T.; Cao, Z.; Zheng, H.; Xiao, J. Q.; Jiao, F.; Chen, J. G. Highly porous non-precious bimetallic electrocatalysts for efficient hydrogen evolution. *Nat. Commun.* **2015**, *6*, No. 6567.
(29) Qiu, H.; Dong, X.; Huang, X. Retracted article: Design of nanoporous metals with bimodal pore size distributions for enhanced biosensing. *Nanoscale* **2012**, *4*, 4492−4497.
(30) Pham, Q. N.; Shao, B.; Kim, Y.; Won, Y. Hierarchical and Well-Ordered Porous Copper for Liquid Transport Properties Control. *ACS Appl. Mater. Interfaces* **2018**, *10*, 16015−16023.
(31) Luo, Z.; Xu, J.; Yuan, B.; Hu, R.; Yang, L.; Gao, Y.; Zhu, M. 3D Hierarchical Porous Cu-Based Composite Current Collector with Enhanced Ligaments for Notably Improved Cycle Stability of Sn Anode in Li-Ion Batteries. *ACS Appl. Mater. Interfaces* **2018**, *10*, 22050−22058.
(32) Zhang, S.; Xing, Y.; Jiang, T.; Du, Z.; Li, F.; He, L.; Liu, W. A three-dimensional tin-coated nanoporous copper for lithium-ion battery anodes. *J. Power Sources* **2011**, *196*, 6915−6919.
(33) Song, R.; Zhang, L.; Zhu, F.; Li, W.; Fu, Z.; Chen, B.; Chen, M.; Zeng, H.; Pan, D. Hierarchical Nanoporous Copper Fabricated by One-Step Dealloying Toward Ultrasensitive Surface-Enhanced Raman Sensing. *Adv. Mater. Interfaces* **2018**, *5*, No. 1800332.
(34) Zhang, H.; Pan, Q.; Zhang, H. Multi-scale porous copper foams as wick structures. *Mater. Lett.* **2013**, *106*, 360−362.
(35) Shin, H.-C.; Liu, M. Copper Foam Structures with Highly Porous Nanostructured Walls. *Chem. Mater.* **2004**, *16*, 5460−5464.
(36) Liu, H.; Wang, E.; Zhang, Q.; Renb, Y.; Guo, X.; Wang, L.; Li, G.; Yu, H. Unique 3D nanoporous/macroporous structure Cu current collector for dendrite-free lithium deposition. *Energy Storage Mater.* **2019**, *17*, 253−259.
(37) Zou, L.; Ge, M.; Zhao, C.; Meng, Q.; Wang, H.; Liu, X.; Lin, C. H.; Xiao, X.; Lee, W. K.; Shen, Q.; Chen, F.; Chen-Wiegart, Y. K. Designing Multiscale Porous Metal by Simple Dealloying with 3D Morphological Evolution Mechanism Revealed via X-ray Nanotomography. *ACS Appl. Mater. Interfaces* **2020**, *12*, 2793−2804.
(38) Lobanov, S. S.; Daly, J. A.; Goncharov, A. F.; Chan, X.; Ghose, S. K.; Zhong, H.; Ehm, L.; Kim, T.; Parise, J. B. Iodine in Metal-Organic Frameworks at High Pressure. *J. Phys. Chem. A* **2018**, *122*, 6109−6117.
(39) Duan, Y.; Yang, L.; Zhang, M.-J.; Chen, Z.; Bai, J.; Amine, K.; Pan, F.; Wang, F. Insights into Li/Ni ordering and surface reconstruction during synthesis of Ni-rich layered oxides. *J. Mater. Chem. A* **2019**, *7*, 513−519.
(40) Chen-Wiegart, Y.-c. K.; Camino, F. E.; Wang, J. Sample preparation of energy materials for X-ray nanotomography with micromanipulation. *ChemPhysChem* **2014**, *15*, 1587−1591.
(41) Ge, M.; Coburn, D. S.; Nazaretski, E.; Xu, W.; Gofron, K.; Xu, H.; Yin, Z.; Lee, W.-K. One-minute nano-tomography using hard X-ray full-field transmission microscope. *Appl. Phys. Lett.* **2018**, *113*, No. 083109.
(42) Gürsoy, D.; De Carlo, F.; Xiao, X.; Jacobsen, C. TomoPy: a framework for the analysis of synchrotron tomographic data. *J. Synchrotron Radiat.* **2014**, *21*, 1188−1193.
(43) O'Mara, A.; King, A. E.; Vickers, J. C.; Kirkcaldie, M. T. K. ImageSURF: An ImageJ Plugin for Batch Pixel-Based Image

https://dx.doi.org/10.1021/acsanm.0c01163
ACS Appl. Nano Mater. XXXX, XXX, XXX−XXX

Segmentation Using Random Forests. *J. Open Res. Software* **2017**, *5*, 31.
(44) Collins, J. M.; King, A. E.; Woodhouse, A.; Kirkcaldie, M.; Vickers, J. Age moderates the effects of traumatic brain injury on beta-amyloid plaque load in APP/PS1 mice. *J. Neurotrauma* **2019**, *36*, 1876−1889.
(45) Chen-Wiegart, Y.-c. K.; DeMike, R.; Erdonmez, C.; Thornton, K.; Barnett, S. A.; Wang, J. Tortuosity characterization of 3D microstructure at nano-scale for energy storage and conversion materials. *J. Power Sources* **2014**, *249*, 349−356.
(46) Münch, B.; Holzer, L. Contradicting Geometrical Concepts in Pore Size Analysis Attained with Electron Microscopy and Mercury Intrusion. *J. Am. Ceram. Soc.* **2008**, *91*, 4059−4067.
(47) Bae, C. J.; Erdonmez, C. K.; Halloran, J. W.; Chiang, Y. M. Design of battery electrodes with dual-scale porosity to minimize tortuosity and maximize performance. *Adv. Mater.* **2013**, *25*, 1254−1258.
(48) Erlebacher, J.; Aziz, M. J.; Karma, A.; Dimitrov, N.; Sieradzki, K. Evolution of nanoporosity in dealloying. *Nature* **2001**, *410*, 450−453.

https://dx.doi.org/10.1021/acsanm.0c01163
ACS Appl. Nano Mater. XXXX, XXX, XXX−XXX